CHEMISTRY OF MATERIALS

pubs.acs.org/cm

Article

Spontaneous Hetero-attachment of Single-Component Colloidal Precursors for the Synthesis of Asymmetric Au−Ag_2X (X = S, Se) Heterodimers

Mengxi Lin, Guillem Montana, Javier Blanco, Lluís Yedra, Heleen van Gog, Marijn A. van Huis, Miguel López-Haro, José Juan Calvino, Sònia Estradé, Francesca Peiró, and Albert Figuerola*

Cite This: *Chem. Mater.* 2022, 34, 10849−10860

Read Online

ACCESS | Metrics & More | Article Recommendations | Supporting Information

ABSTRACT: Finding simple, easily controlled, and flexible synthetic routes for the preparation of ternary and hybrid nanostructured semiconductors is always highly desirable, especially to fulfill the requirements for mass production to enable application to many fields such as optoelectronics, thermoelectricity, and catalysis. Moreover, understanding the underlying reaction mechanisms is equally important, offering a starting point for its extrapolation from one system to another. In this work, we developed a new and more straightforward colloidal synthetic way to form hybrid Au−Ag_2X (X = S, Se) nanoparticles under mild conditions through the reaction of Au and Ag_2X nanostructured precursors in solution. At the solid−solid interface between metallic domains and the binary chalcogenide domains, a small fraction of a ternary $AuAg_3X_2$ phase was observed to have grown as a consequence of a solid-state electrochemical reaction, as confirmed by computational studies. Thus, the formation of stable ternary phases drives the selective hetero-attachment of Au and Ag_2X nanoparticles in solution, consolidates the interface between their domains, and stabilizes the whole hybrid Au−Ag_2X systems.

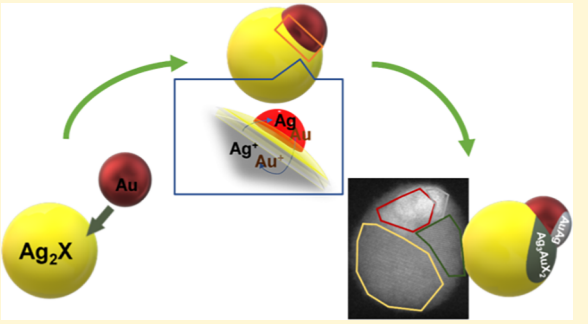

Producing nanoscale heterostructures in which the distinct nanomaterial domains are coupled together through solid−solid interfaces enables multifunctionality in a single nanosystem.[1,2] Beyond the size, shape, and composition-tunable optical, magnetic, electronic, and catalytic properties of single-component nanomaterials, the tunability of nanoscale heterostructures can be further expanded by controlling the interface, spatial arrangements, and configurations among different domains.[3] The combined properties were also found to often surpass the functionality of individual components due to the synergistic effect.[4] For instance, integrating CdS and MoS_2 into one system not only enlarges the light absorption spectra in comparison to the individual components but also enhances the photochemical performance as photocatalysts.[5] The transformation from uniform core@shell to nano-dumbbell Au−CdSe hybrids is another example illustrating the importance of the hybrid configuration and interface design, resulting in a wide optical response range across visible and near-infrared regions,[6] which could not be achieved by simply mixing the two materials.[7]

In order to achieve such sophisticated colloidal hetero-structured nanoparticles (NPs) with programmable features, the seed-mediated growth method is one of the most extensively used approaches whereby the pre-existing NPs serve as seeds and allow the subsequent nucleation and growth of another material directly on their surfaces.[8] This approach opens the door to the synthesis and study of a large variety of hybrid systems.[9−12] However, when it comes to the design of some specific hybrid NPs, this approach begins to show its flaws, giving rise to its vulnerability in the multiple-step process. In other words, the final product is highly influenced by numerous reaction parameters and some underlying mechanisms still remain unknown or they are still difficult to control.[13] For example, the size and morphology of seed particles influence deeply the nucleation and growth processes of second domains, and on the other hand, the seeds themselves are very sensitive to the reaction conditions such as temperature, surfactants, and solvent.[13,14]

Given all these challenges, alternative methods for synthesis of complex hybrid NPs are highly desirable so that the variety of synthetic tools could be further expanded to fulfill the needs of the scientific community. Innovative synthetic routes proposed in the past years suggest the use of pre-made nanoparticles as precursor alternatives for the synthesis of

Received: June 21, 2022
Revised: November 23, 2022
Published: December 12, 2022

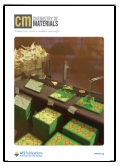

https://doi.org/10.1021/acs.chemmater.2c01838
Chem. Mater. 2022, 34, 10849−10860

further nanostructures in such a way that the final products are obtained simply by the attachment of pre-synthesized NPs in solution (or by their transformation) and new solid domains do not need to nucleate.[15,16] Soft reaction conditions are often required in these cases compared to traditional solid-state chemistry, considering the increased reactivity of nanoparticles with high surface-to-volume ratios and short atomic diffusion distances due to their small dimensions. Additionally, compared to standard bottom-up wet methods, the use of nanoparticles as starting materials often avoids both (1) the need for significant amounts of surfactant molecules in the solution acting as stabilizers and size and shape-driving agents and (2) the presence of metallic counteranions that might interfere in the reaction as well as compromise the physical performance of the final material.

Cation exchange (CE) reactions in solution are one example of these new types of synthetic approaches. This is one of the most useful post-synthetic transformations, and it has been widely applied for preparing heterostructured NPs, resulting in good preservation of the morphology of initial materials while the compositions are modified.[8,17−20] In a CE reaction, a material acts as a host lattice and permits the exchange reaction between its own cations and other guest cations. Over the last years, several new and compositionally complex NPs have been successfully obtained, such as $Cu_5FeS_4/Cu_{2-x}S/Cu_5FeS_4$ nanosandwiches with exciting physicochemical properties,[21] $(CuGaIn)S_2$ nanocrystals (NCs) with 10-fold higher photoluminescence quantum yields compared to their parental nanostructures,[22] and various metal-doped perovskite quantum dots.[23,24]

In the previous publications of our group, gradual cation exchange reactions between gold chloride and silver chalcogenide NPs have been studied.[25,26] The partial exchange of Ag^+ by Au^+ cations in the silver chalcogenide lattice entails the formation of ternary phases, a process that is kinetically favored, and thus it occurs fast at room temperature and without the need for additional ligands except for those required to solubilize the gold molecular precursor and stabilize the silver chalcogenide NPs in organic apolar solvents. The easiness of this cation exchange reaction suggests a high stability for the ternary products formed.

The high affinity between gold and silver chalcogenide lattices observed in our previous works made us consider one further step: here, we describe the reaction of solely nanostructured materials, that is, Au NPs and Ag_2X (X = S, Se) NPs, leading to heterostructured or hybrid Au−Ag_2X NPs. The reactions occur at room temperature and atmospheric pressure in solution without the addition of surfactants or molecular precursors. Experimental data and calculations confirm that the possibility to form ternary phases at the interface between pre-made Au and Ag_2X solid NPs is the main driving force for the formation of the hybrids. Our results point to an electrochemical replacement mechanism occurring solely through the solid interface between the two inorganic sections after their hetero-attachment.

EXPERIMENTAL SECTION

Chemicals. Sulfur powder (S, 99.99%), silver chloride (AgCl, 99.9%), selenium powder (Se, 99.9%), and tri-n-octylphosphine (TOP, 97%) were obtained from Strem Chemicals. Silver nitrate ($AgNO_3$, 99%), gold(III) chloride trihydrate ($HAuCl_4{\cdot}3H_2O$, ≥99.9%), oleylamine (OLAm, 70%), tri-n-octylphosphine oxide (TOPO, 99%), sodium borohydride ($NaBH_4$, 98%), tetrahydrofuran (THF, 99%), octadecene (ODE, 90%), and toluene (99.9%), 11-mercaptoundecanoic acid (MUA, 95%), and sodium citrate tribasic dihydrate were purchased from Sigma-Aldrich. Ethanol (EtOH, 96%) and acetone (99.5%) were obtained from Panreac.

Synthesis of Au NPs (3.5 nm). A mixture of 20 mg (0.1 mmol) of $HAuCl_4{\cdot}3H_2O$ and 2 mL of ODE was degassed in three cycles of vacuum/N_2 at room temperature followed by additions of 100 μL of TOP and 100 μL of OLAm under a N_2 atmosphere. Subsequently, a suspension of 6 mg (0.16 mmol) of $NaBH_4$ and 0.5 mL of THF was injected into the reaction mixture, and the mixture was reacted under stirring for 2 h. The solution was cleaned first by adding some milliliters of toluene to remove the excess of $NaBH_4$ and centrifuged for 10 min at 4500 rpm. Then, the NPs were washed with acetone, centrifuged for 30 min at 6000 rpm, and re-dispersed in 4 mL of toluene with a concentration of 29.96 μmol/L Au NPs.

Synthesis of Ag_2S NPs (16 nm). The synthesis was adapted from the work of Yang and co-workers.[27] Briefly, 17 mg (0.1 mmol) of $AgNO_3$, 8 mg of S (0.25 mmol), and 8 mL of OLAm were placed in a three-necked flask, and the mixture was purged three times by vacuum-N_2 cycles. Afterward, the reaction temperature was raised to 160 °C under a N_2 atmosphere. After 20 min of reaction, the heating was removed, and the solution was left to cool down to room temperature naturally. The final dark brown solution was washed once with EtOH and centrifuged for 4 min at 4500 rpm. The final NPs were re-dispersed in 4 mL of toluene for further use. The final solution is dark green with a concentration of 2.7 μmol/L Ag_2S NPs.

Synthesis of Ag_2Se NPs (8 nm). The synthesis of Ag_2Se NPs followed the procedure published by Sahu and co-workers.[28] Briefly, two precursor solutions were prepared first in the glove box: 474 mg (6 mmol) of Se was dissolved in 6 mL of TOP, and 572 mg (4 mmol) of AgCl was dissolved in 4 mL of TOP. Afterward, a solution of 7.8 g of TOPO and 6.6 mL of OLAm was degassed under vacuum at 120 °C for 30 min, and the temperature was then raised to 180 °C under a N_2 atmosphere followed by the injection of Se-TOP. Once the temperature was back to 180 °C, the AgCl-TOP was injected swiftly. The heating was stopped after 20 min, and the solution was cooled down naturally. Five milliliters of toluene was added into the reaction mixture at 50 °C to prevent the solidification of the solvent. Finally, the solution was washed twice with EtOH, centrifuged for 4 min at 4500 rpm, and re-dispersed with 4 mL of toluene, resulting in a dark brown solution with a concentration of 3.6 μmol/L Ag_2Se NPs.

Phase Transfer of Ag_2S and Au from Toluene to Water. Twenty milligrams (0.1 mmol) of MUA was added into a 1 mL dispersion of Ag_2S NPs and Au NPs in toluene. Subsequently, the dispersions were brought to sonication for 15 min until the precipitates appeared at the bottom of the vials. Afterward, 1 mL of Milli-Q water was tuned to slightly basic (pH in between 7 and 8) by adding sodium citrate and added into both mixtures. Finally, the water phases for both samples were extracted and then followed with sonication for 10 min.

Synthesis of Au−Ag_2S and Au−Ag_2Se Hybrid NPs. In order to obtain both hybrid systems, a simple synthetic procedure was developed. For the Au−Ag−S system, 350 μL of the Ag_2S colloidal suspension was mixed with 50 μL of the Au suspension at room temperature for 24 h. In the case of the Au−Ag−Se system, 65 μL of the Au suspension was mixed with 350 μL of the Ag_2Se suspension. Both reactions were stopped by adding an antisolvent of acetone followed by centrifugation for 4 min at 4500 rpm. Both final NPs were re-dispersed in toluene.

CHARACTERIZATION METHODS

Transmission Electron Microscopy (TEM). All of the samples were prepared for observation by transmission electron microscopy (TEM) by dispersion in toluene followed by sonication. A droplet was subsequently deposited on a copper TEM grid covered with holey carbon. For morphological characterization, the samples were examined in a Tecnai Spirit TEM working at 120 kV. The samples were further observed in a JEOL 2010F TEM at 200 kV and in a ThermoFisher TITAN Themis at 200 kV. The electron tomography

https://doi.org/10.1021/acs.chemmater.2c01838
Chem. Mater. 2022, 34, 10849−10860

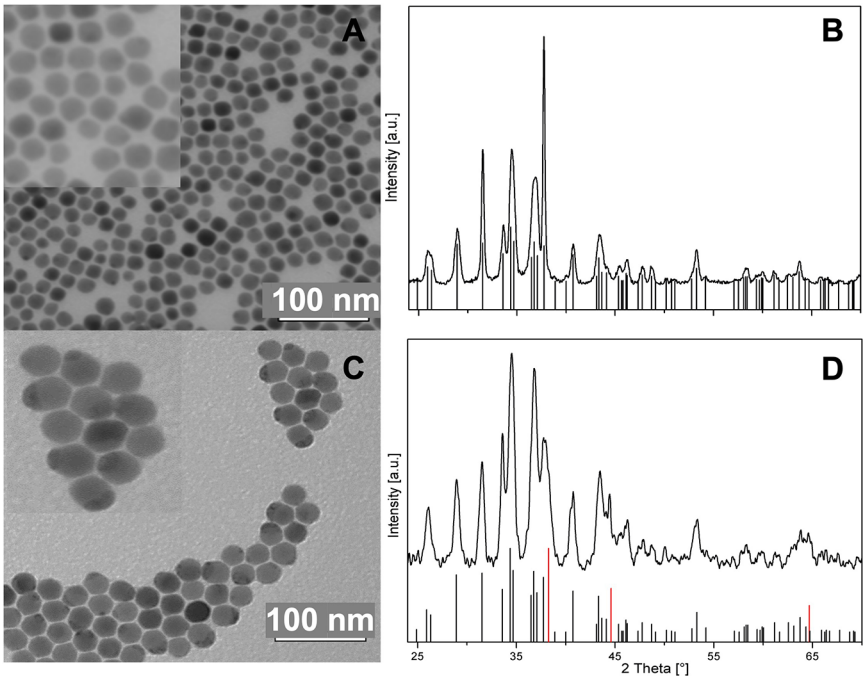

Figure 1. (A) TEM micrograph of Ag_2S NPs. (B) XRD spectrum of the Ag_2S NPs and Ag_2S (JCPDS no. 00-024-0715, black) reference pattern. (C) TEM images of Au−Ag_2S hybrid NPs. (D) XRD spectrum of the Au−Ag_2S hybrid NPs, Ag_2S (JCPDS no. 00-024-0715, black), and Au (JCPDS no. 00-001-1172, red) reference pattern.

experiments were conducted by acquiring a projection series from −70 to +70 degrees with an angular step of 5° in the same TITAN Themis at 200 kV. The X-EDS spectrum images were also acquired in the TITAN Themis at 200 kV via the Super-X in-column detector.

The optical characterization was carried out in a Cary 100 SCAN 388 Varian UV−vis spectrophotometer with quartz cuvettes. The instrument was commanded with Varian UV v. 333.

X-ray diffraction (XRD) spectra were acquired with a PANalytical X′pert Pro MPD Alpha 1 diffractometer operating in a $\theta/2\theta$ geometry at 45 kV, 40 mA, and λ= 1.5406 Å (Cu $K_{\alpha 1}$). Thin layers of samples were prepared by drop-casting and evaporation of the solvent in a monocrystalline Si holder of 15 mm in diameter and 0.15 mm in height. Scans in the range of 2θ = 4−100° were run at a step size of 2θ= 0.017° and 100 s per step. The data were treated with X'pert HighScorePlus software.

The composition and concentration of the NP solutions were determined by inductively coupled plasma-atomic emission spectroscopy (ICP-ES). The measurements were carried out by an Optima 3200 RL PerkinElmer spectrometer. For those measurements, 50 μL of solutions was precipitated in MeOH and redispersed in $CHCl_3$. The solution was evaporated in an oven overnight at 90 °C. Before the vial was sealed, 2.5 mL of aqua regia was added to the precipitate and then heated to 90 °C for 72 h. The resulting solution was transferred to a 25 mL volumetric flask and diluted with Mili-Q water.

Zeta potentials for the above-described Ag_2S and Au (3.5 nm) NPs were monitored using a ZetasizerNano ZS (Malvern Instruments Ltd., Germany).

Computational Section. To gain insight into the relative stability of the observed phases and to determine their electronic band gap, density functional theory (DFT) calculations were conducted using the Vienna ab initio simulation package (VASP).[29,30] The projector augmented wave (PAW) method[31,32] was applied in combination with the generalized gradient approximation (GGA) by Perdew, Burke, and Ernzerhof (PBE).[33] Settings for the energy cutoff of the electronic wavefunctions and for the density of the k-mesh were tested on elemental Ag, elemental Au, and orthorhombic Ag_2Se to ensure energy convergence within 0.5 meV/atom. Settings meeting this criterion were subsequently applied to all phases. Consequently, all structures were calculated using energy cutoffs of 550 eV for the valence electronic wavefunctions and 770 eV for the augmentation wavefunctions. For the metallic systems of Ag, Au, and Ag_xAu_y, the required k-mesh was 28 × 28 × 28 for the conventional fcc unit cells. For all compounds of M_2S and M_2Se (M = Ag, Au), the k-meshes were set to have a linear k-spacing of less than 0.028 $Å^{-1}$ in any reciprocal lattice direction. Energy convergence criteria of 10^{-6} and 10^{-5} eV were used for the electronic and ionic loops, respectively. Table S3 provides an overview of all calculated phases with the number of atoms per unit cell and the k-meshes used in the calculations. During the GGA-PBE calculations, both the cell dimensions and the atomic coordinates were fully relaxed to obtain the lowest-energy configurations. The calculated lattice parameters are also provided in Table S3.

The DFT calculations are valid for a temperature of 0 K and a pressure of 0 Pa. Spin−orbit coupling effects were not taken into account. For calculation of Ag−Au mixed phases, ordered Ag_3Au_1 and Ag_1Au_1 compounds were calculated within the conventional fcc unit cell. The entropy of mixing in the Ag−Au system, which is known to form a continuous solid solution, has therefore been ignored as well. For the AgAuS *petrovskaite* phase, there is some discussion in the literature about the exact composition as the 9e Wyckoff position is reported to be 1/3-occupied by Ag atoms and 2/3-occupied by Au atoms.[34] To cover a wider compositional range, configurations with all 9e Wyckoff positions occupied by either Ag or Au atoms were also calculated within the *petrovskaite* phase (yielding compositions of $Ag_{30}Au_{18}S_{24}$ and $Ag_{21}Au_{17}S_{24}$), but these were found to be energetically relatively unfavorable.

As DFT calculations typically lead to severe underestimation of the size of the electronic band gap, hybrid DFT calculations were also performed using the Heyd−Scuseria−Ernzerhof HSE06 functional[35] with 25% of Hartree-Fock exchange. The HSE06 calculations were performed on the relaxed configurations as found from GGA-PBE without any further relaxation.

RESULTS AND DISCUSSION

Ag_2S Precursor NPs and Au−Ag_2S Hybrid NPs. For the synthesis of the Au−Ag_2S hybrid system, Ag_2S NPs and Au NPs were used as precursors for further mixing. The Ag_2S

https://doi.org/10.1021/acs.chemmater.2c01838
Chem. Mater. 2022, 34, 10849−10860

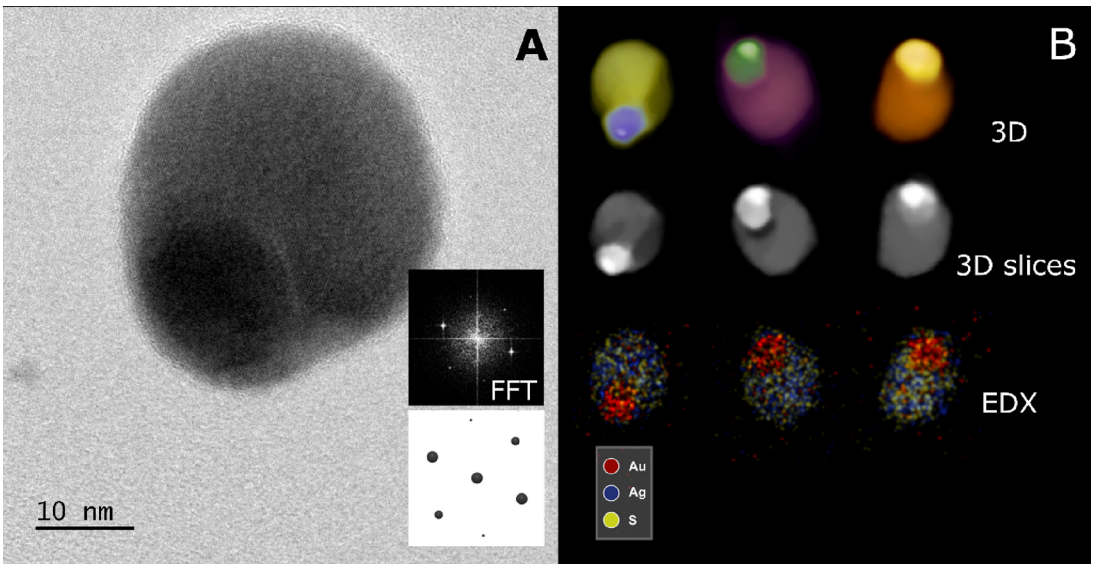

Figure 2. Au−Ag_2S hybrid NP characterization. (A) HRTEM image with FFT as an inset. The crystal could be indexed as a [352]-oriented acanthite (see theoretical pattern below the FFT). (B) Electron tomographic reconstructions of three particles (shown as volume renderings in arbitrary colors) with an orthoslice through the volume of each particle and elemental mappings extracted from X-EDS spectra.

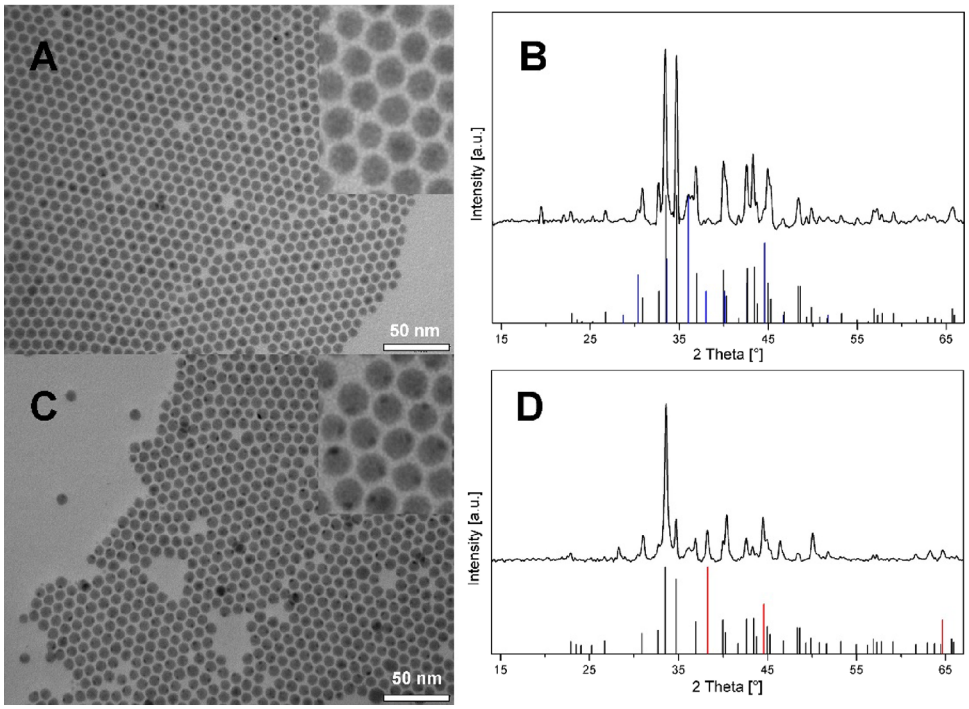

Figure 3. (A) TEM micrograph of Ag_2Se NPs. (B) XRD spectrum of the Ag_2Se NPs, β-Ag_2Se (JCPDS no. 00-024-1041, black) reference pattern, and t-Ag_2Se calculated (blue) pattern.[28] (C) TEM images of Au−Ag_2Se hybrid NPs. (D) XRD spectrum of the Au−Ag_2Se hybrid NPs, Ag_2Se (JCPDS no. 00-024-1041, black), and Au (no. JCPDS 00-001-1172, red) reference pattern.

precursors were prepared by a heat-up method published by Wang and co-workers,[27] which is a one-pot reaction consisting of $AgNO_3$, S, and oleylamine as both a surfactant and solvent heated up to 160 °C under an inert atmosphere, resulting in quite homogeneous faceted NPs with a diameter of 16 nm, as shown in the TEM micrograph in Figure 1A. The XRD spectrum in Figure 1B showed the formation of Ag_2S, crystallizing in an acanthite monoclinic structure as expected, that is stable below a temperature of 177 °C.[36] A small fraction of NPs contained an additional smaller and darker domain at their surface, as observed by low-resolution TEM micrographs. They were further analyzed by high-resolution TEM (HRTEM), as shown in Figure S1, and they were identified as metallic Ag appearing on the surface of a few monoclinic Ag_2S NPs.

The formation of Au−Ag_2S heterodimers was achieved by simply mixing the two pre-synthesized Ag_2S NPs and Au NPs in solution at room temperature. A TEM micrograph of the precursor Au NPs is shown in Figure S2: they exhibit a spherical shape with an average diameter of 3.5 nm. The TEM micrograph in Figure 1C shows the nanostructures obtained upon mixture of the NPs. A clear second domain with a dark

https://doi.org/10.1021/acs.chemmater.2c01838
Chem. Mater. 2022, 34, 10849−10860

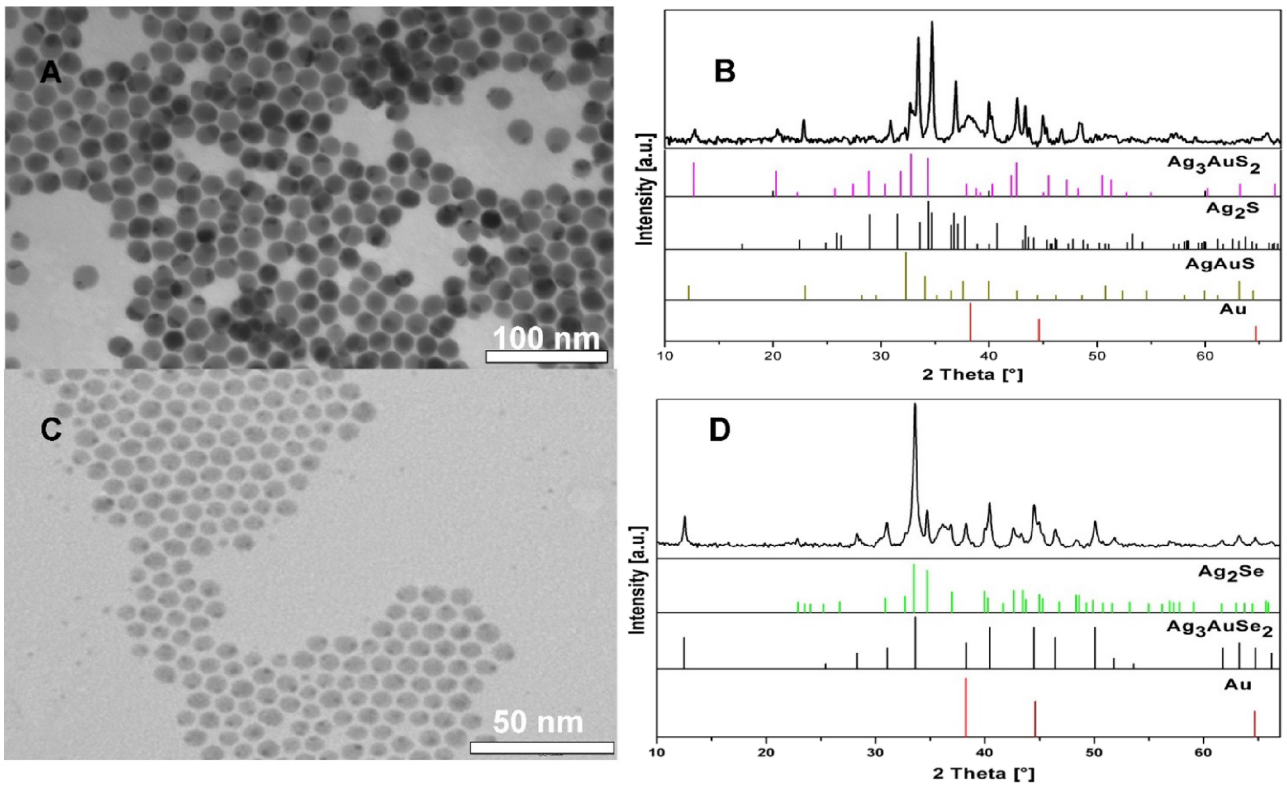

Figure 4. (A) TEM micrograph of the Au−$AuAg_3S_2$−Ag_2S sample. (B) XRD spectrum of Au−Ag_3AuS_2−Ag_2S, Ag_2S (JCPDS no. 00-024-0715, black), AgAuS (JCPDS no. 00-038-0396, olive), Ag_3AuS_2 (JCPDS no. 01-072-0390, pink), and Au (JCPDS no. 00-001-1172, red) reference pattern. (C) TEM images of the Au−Ag_3AuSe_2−Ag_2Se sample. (D) XRD spectrum of Au−$AuAg_3Se_2$−Ag_2Se, Ag_2Se (JCPDS no. 00-024-1041, black), Ag_3AuSe_2 (JCPDS no. 00-025-0367, green), and Au (JCPDS no. 00-001-1172, red) reference pattern.

contrast is observed on almost each surface of the faceted Ag_2S NPs. The XRD, shown in Figure 1D, reveals the presence of cubic metallic Au in the samples through the extra "shoulder" peak at 38.2° and another peak at 44.6° that are the two most intense peaks belonging to cubic metallic Au.

The HRTEM image and the result of STEM-EDS elemental maps in Figure 2A,B reflect the same results derived previously by XRD analysis. The volume renderings in Figure 2B obtained through electron tomography only show the presence of two domains in every particle. The two intensities observed in the images correspond to Ag_2S for the lowest intensity and Au for the highest. The slices through the reconstructed volume show how the Au part is partially physically embedded in the Ag_2S, and the EDX maps show the confinement of Au exclusively to the bright domain. The HRTEM image in Figure 2A shows atomic planes that could be indexed as acanthite Ag_2S, thus confirming the nature of the largest domain.

Ag_2Se Precursor NPs and Au−Ag_2Se Hybrid NPs. The synthetic approach begins first with the preparation of monodisperse Ag_2Se NPs as precursors by a hot-injection method developed by Yang and co-workers.[37] Figure 3A shows the TEM micrograph of as-synthesized Ag_2Se NPs with a hexagonal shape and with an average diameter of 8 nm. The XRD pattern of the sample in Figure 3B indicates that the NPs crystallized mainly in the orthorhombic phase (β-Ag_2Se), which is one of the three known crystallographic phases for Ag_2Se. The others are in the cubic phase (α-Ag_2Se), which is stable above 135 °C, and metastable tetragonal phase (τ-Ag_2Se), exclusively observed in nanocrystals or polycrystalline Ag_2Se contained in thin films.[38] The latter phase can also be identified in the XRD spectrum as a minor product. The formation of Au−Ag_2Se NPs is performed analogously by the same strategy used for the preparation of hybrid Au−Ag_2S NPs in the previous section. The final product was observed by TEM and a general view is shown in Figure 3C. In comparison with the TEM images of Ag_2Se precursors, a small dark spot appears attached on the surface of almost every hexagonally shaped Ag_2Se NP, corresponding to metallic Au domains (as observed in Figure S3), indicating the formation of hybrid Au−Ag_2Se systems. The corresponding XRD spectrum in Figure 3D confirms our assumption, showing that some additional peaks arise besides those belonging to orthorhombic Ag_2Se, which can be assigned to cubic metallic Au: see its most intense and characteristic diffraction peak at 38.2°, which is attributed to the Au(111) set of equivalent planes.

Au−Ag_3AuS_2−Ag_2S NPs and Au−Ag_3AuSe_2−Ag_2Se NPs. The complexity of crystalline phases in those two Au−Ag−S and Au−Ag−Se systems can be further tuned by doubling the amounts of Au NPs in both reactions. Although the TEM micrographs at low magnification of both samples (Figure 4A,C) are very similar to those of the previous hybrid NPs (Au−Ag_2S and Au−Ag_2Se) in morphology and size, their corresponding XRD spectra (Figure 4B,D) show that both samples are not composed of only the binary precursors and metallic Au. The extra peaks of the Au−Ag−S sample in the XRD spectrum (Figure 4B) show the formation of the cubic Ag_3AuS_2 phase besides the acanthite Ag_2S. Moreover, a monoclinic lattice from another AgAuS ternary material is also very likely contained in the sample mainly through two assignable peaks at 22.9° and 39.9°, although this cannot be fully confirmed due to the fact that the reference pattern of AgAuS always overlaps with one or two other reference

https://doi.org/10.1021/acs.chemmater.2c01838
Chem. Mater. 2022, 34, 10849−10860

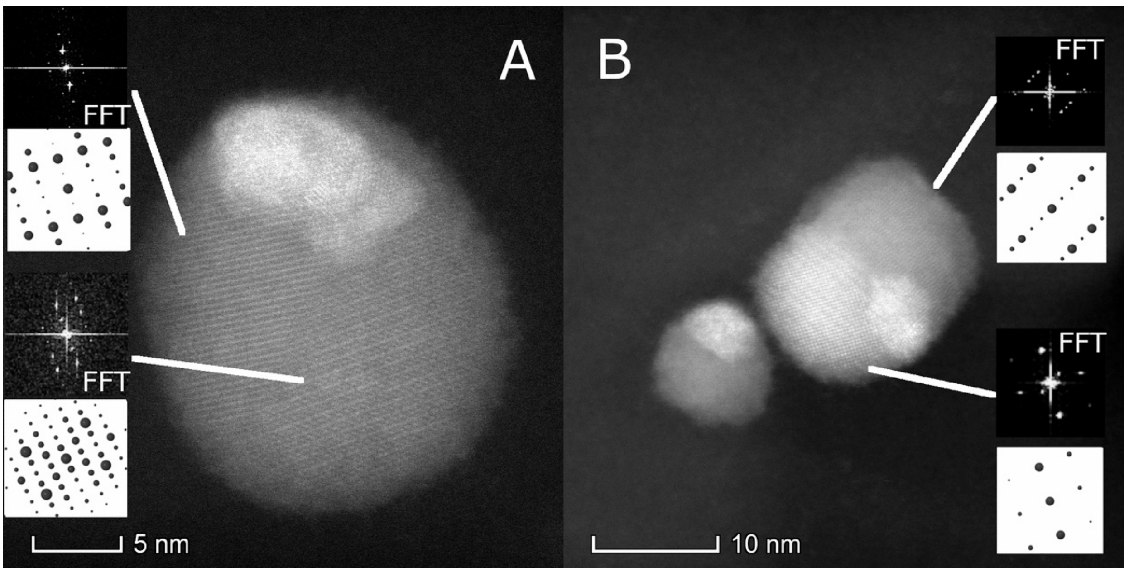

Figure 5. HRSTEM images of (A) Au−Ag_3AuS_2−Ag_2S NPs and (B) Au−Ag_3AuSe_2−Ag_2Se NPs. The FFTs of the two biggest crystallites observed in the particles have been indexed as [101] Ag_3AuS_2 (top inset) and [101] Ag_2S (bottom inset) for A and [212] Ag_3AuSe_2 (top inset) and [241] Ag_2Se (bottom inset) for B. The brightest crystal corresponds to gold.

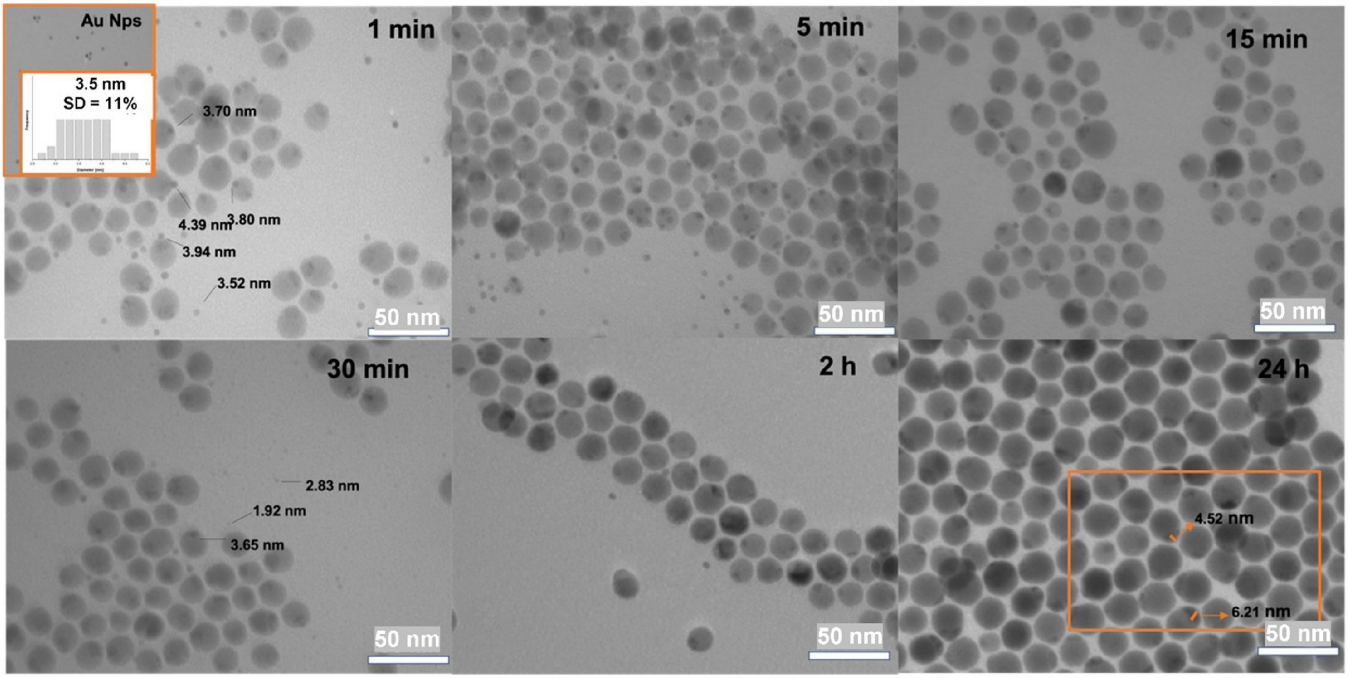

Figure 6. TEM images of aliquots at specific times along the reaction between Ag_2S NPs and Au NPs.

patterns (Ag_3AuS_2 and Ag_2S). By analyzing the XRD pattern of the selenium-containing sample (Au−Ag−Se), a few relative intense peaks located at 41.3°, 28.3°, and especially 12.5°, representing quite a large interplanar distance, can be easily assigned to the (310), (420), and (111) sets of planes in the cubic Ag_3AuSe_2 crystal structure. In Figure 5, one HR-HAADF image per material is shown with three crystalline regions each. As observed previously, the smallest and brightest region corresponds to metallic Au. Upon close examination, the other crystallites can be indexed as the binary and ternary phases of Au−Ag_3AuS_2−Ag_2S (A) and Au−Ag_3AuSe_2−Ag_2Se (B), which corroborates and refines the XRD observations. In both kinds of particles, the ternary and binary compounds are in contact with the gold domain, but the ternary ones share a vaster interface with it.

Study of Influencing Factors and the Reaction Mechanism. Analogous reactions of Ag_2S NPs have been performed with Au NPs of different sizes, with Au nanorods (NRs) and with hydrophilic Ag_2S and Au NPs in order to unveil the size, shape, ligand, and solvent dependence of the reaction studied. The use of 11 nm Au NPs as precursors instead of 3.5 nm ones did not present any change in the final product obtained besides the obvious fact of obtaining Au−Ag_2S dimers with larger Au domains, as shown by TEM and XRD in Table S1. However, using 25 nm Au NPs as precursors led to an irreversible aggregation of Au after long reaction

https://doi.org/10.1021/acs.chemmater.2c01838
Chem. Mater. 2022, 34, 10849−10860

Scheme 1. Heterodimer Formation Mechanism[a]

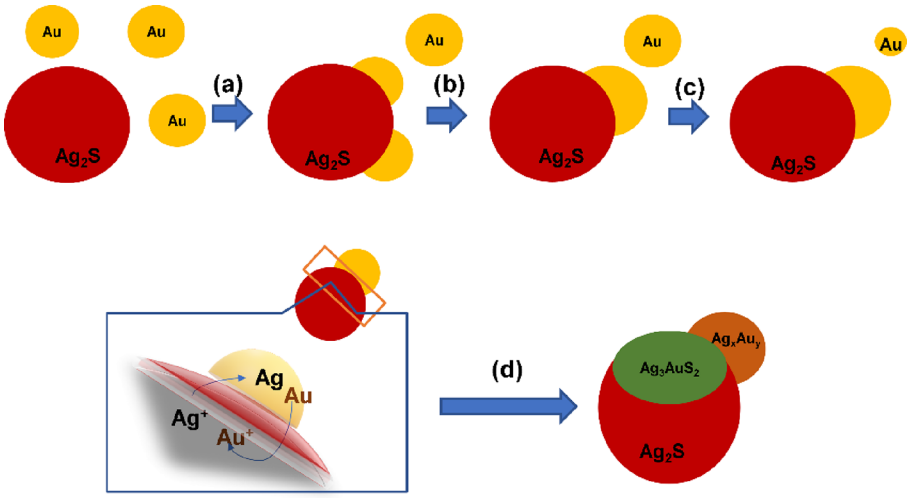

[a](a) NP hetero-attachment, (b) Au NP coalescence at the chalcogenide surface, (c) solution-mediated Au NP ripening, and (d) solid interface-confined electrochemical replacement.

times, and no hybrid Au−Ag_2S NPs could be observed, as indicated in Table S1 and Figure S4, through TEM, XRD, and EDX analysis. The use of anisotropically shaped Ag_2S NRs instead of spherical NPs neither presented any inconvenience for the occurrence of the reaction as shown in Figure S5. Lastly, ligand exchange reactions were performed in both nanostructured precursors, resulting in water-dispersed 3.5 nm Au NPs and 16 nm Ag_2S NPs, both capped with MUA instead of OLAm. Subsequently, both NPs were mixed under the same reaction conditions as in the initially reported synthesis but in water. As a result, analogous dimer-like NPs were formed, as shown in Table S1. All in all, these additional experiments suggest that the current method is not restricted to a certain type of ligand, solvent, and shape of pre-made NPs. However, the methodology seems to be applicable only for small or medium-sized Au NPs (up to 11 nm based on the experiments) since relatively large Au NPs tend to aggregate with each other rather than react with Ag_2S NPs. It is also interesting to note that the formation of ternary phases (Ag_3AuS_2, AgAuS, or Ag_3AuSe_2) has been confirmed in all samples prepared both by bulk XRD and local HRTEM analysis, as shown in Table S1 and Figure S6.

The heterodimers found in these samples are very similar to those obtained through standard seeded-growth methods, as reported in our previous work, in terms of size, geometry, and homogeneity.[9,26] Nevertheless, this new procedure requires no phase transfer of Au(III) ions from water to toluene since pre-made Au NPs are used as precursors. Additionally, the heterogeneous nucleation of Au domains on the surface of chalcogenide NPs occurring in seeded-growth approaches requires the presence of surfactant-stabilizing molecules in considerable amounts, which might not only present an issue in terms of contamination for their characterization, but more importantly, their electronic and catalytic performance can fade.

The reaction mechanism has been investigated through an experiment in which Ag_2S NPs and Au NPs were mixed following the method described in the Experimental Section, and aliquots were withdrawn from the reaction flask at specific time lapses and analyzed under the TEM. Figure 6 shows how the aliquot taken at 1 min contains single-component Ag_2S and Au NPs as major products, although a considerable amount of Au−Ag_2S hybrid NPs can be already identified after a short reaction time. In the course of the reaction, the population of hybrid nanostructures becomes significantly larger until every Ag_2S NP is decorated with at least one Au domain, while isolated Au NPs are still observed in the reaction mixture due to the excess of Au NPs added to the reaction medium. Noteworthy, size analysis indicates that Au domains preserve the size of the original precursor NPs for up to ca. 15 min of reaction, both the ones already attached to the semiconductor domain and those still free in the solution. These observations might be seen as an evidence of direct particle hetero-attachment as the single operative mechanism during the formation of solid−solid Au−Ag_2X interfaces, thus confirming the absence of ripening of Au NPs and their heterogeneous nucleation at the surface of Ag_2S. The Au/Ag_2X NP ratio in the reaction medium plays an important role in tuning the size of the final Au domain, as inferred from the Au−Ag_2S NPs with large Au domains seen in Figure 1C where a Au/Ag_2S NP ratio larger than 1 was used, compared to Au−Ag_2Se NPs with smaller Au domains in Figure 3C where the Au/Ag_2Se NP ratio was closer to unity. Indeed, Au−Ag_2S hybrid NPs prepared with a Au/Ag_2S NP ratio close to 2 show many particles with two or even three Au NPs attached during the first 15 min of reaction. Interestingly, for longer reaction times, these multi-domain NPs evolve to dimer-like NPs where the Au domain grows and significantly modifies its initial shape. Simultaneously, the Au NPs that are still free in solution are observed to gradually decrease their size, as confirmed by size analysis. All in all, our experiments point to direct particle hetero-attachment as the single operative mechanism during the formation of solid−solid Au-Ag_2X interfaces at short reaction times, although in those systems where Au/Ag_2X NP ratios larger than 1 are used, the final size of the Au domain in the hybrid NP can be increased through (a) the coalescence of multiple Au NPs already attached at the chalcogenide surface and (b) a solution-mediated ripening process involving free Au NPs in solution used as sacrificial dots, as illustrated in Scheme 1. Based on the data shown in Figure S7, identical conclusions can be extracted from those experiments performed using larger Au NPs as precursors (ca. 11 nm), suggesting that the

https://doi.org/10.1021/acs.chemmater.2c01838
Chem. Mater. 2022, 34, 10849−10860

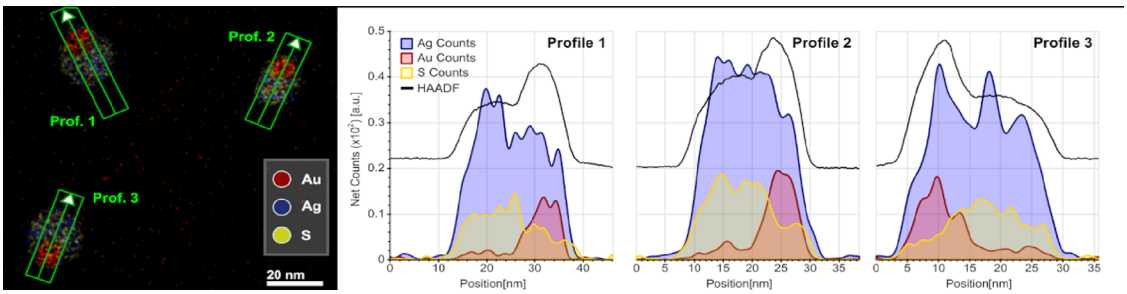

Figure 7. EDX map of three Ag_3AuS_2 particles from which signal profiles have been extracted along the indicated arrows. Note the presence of the Ag signal all over the particle.

reaction mechanism is valid within the full range of sizes for which the reaction occurs, as stated above.

In those experiments with a Au/Ag_2X ratio of above 3, the formation of ternary Ag_3AuX_2 phases is always confirmed after relatively long reaction times. Indeed, ternary domains are strongly confined at the newly formed solid−solid interface between the metallic and the semiconductor sections, suggesting that their formation is strictly related to an interface phenomenon. Additional measurements (Figure 7) indicate the presence of Ag within the metallic Au domains. The EDX elemental profiles extracted along the particles show the presence of Ag all over the analyzed particles. Although not quantifiable, the data confirm the partial reduction of Ag^+ cations from the Ag_2X domain to metallic Ag, which are alloyed with the Au domain. Clearly, the partial reduction and release of Ag^+ cations from the Ag_2X domain is accompanied by the partial oxidation of metallic Au atoms to Au^+ cations that diffuse into the semiconductor to form the observed Ag_3AuX_2 ternary interface, as depicted in Scheme 1 and indicated in the following reaction for the Se-based system:

$$2\,Ag_2Se + 2\,Au \rightarrow Ag_3AuSe_2 + AgAu \quad (1)$$

Thus, it can be concluded that the stabilization of the interface takes place through an interdomain redox reaction at the solid−solid interface followed by atomic diffusion and exchange, occurring only after particle hetero-attachment, leading to the formation of ternary semiconductor phases and metallic alloyed domains. Compared to previous strategies[9,26] where more standard molecular precursors are used for the exchange leading to ternary phases (i.e., $AuCl_3$ instead of Au NPs), the replacement here described occurs exclusively at the interface and can be considered as an intraparticle process: ternary domains grown far apart from the metal−semiconductor interface were never found, suggesting that the solvent is not assisting the replacement through atom diffusion, which is only a solid-phase phenomenon.

Stability of the Ternary Phases. Both Au and Ag_2X precursor NPs are stabilized in toluene by coordinating OLAm, a long-chain hydrocarbon amine. This fact excludes the electrostatic attraction between oppositely charged NPs as a driving force promoting hetero-attachment (asymmetric Au−Ag_2X) versus homo-attachment (symmetric Au−Au or Ag_2X−Ag_2X) of NPs in solution in contrast with previous reports.[39,40] For further evidence, zeta-potential measurements were performed for Au−MUA and Ag_2S−MUA hydrophilic NPs in water, which suffer analogous hetero-attachment upon mixture. Negative zeta-potential values were obtained in both cases, as shown in Table S2. These data indicate that the hetero-attachment occurs regardless of the electrostatic repulsion between Au NPs and Ag_2X NPs in water.

Thus, one may think of surface tension reduction as the main factor facilitating the attachment. However, if this was the only factor to consider, homo-attachment is expected to reduce even more the surface energy in the system compared to hetero-attachment due to the optimal lattice match and chemical affinity in the first case. In all our experiments, no dimer particles made of a single component were ever observed, indicating that the precursor NPs are well isolated and stabilized as colloids by the surfactants at their surface, and no attachment or aggregation is needed to decrease the energy of the system. Moreover, the hetero-attachment observed is not crystallographically oriented, that is, no epitaxial relationship could be found at the interface between the two domains. This is a further indication that there is no specific combination of crystal facets that manages to stabilize a net Au−Ag_2X interface and would be directing the attachment. Consequently, there must be another driving force that leads exclusively to the hetero-attachment observed, which is most likely the ease of the formation of the thermodynamically stable ternary compounds.

The experimental data collected confirm that metallic Au is oxidized to Au^+ while Ag^+ reduces to metallic Ag to form the ternary chalcogenide and the alloy at the interface, respectively. This proceeds spontaneously, although the standard reduction potentials of those metals would dictate the opposite reaction.[41] Recently, Pattadar et al. reported on the observation of the so-called size-dependent antigalvanic replacement between Au NPs and Ag^+ solution where the unfavorable thermodynamic redox process was gaining importance with the decreasing size of the Au NPs.[42] In view of our results, a similar redox replacement is observed, although in the solid state. Additionally, when using differently sized Au NPs (see previous section), it can be concluded that the solid-state redox replacement observed is also size-dependent. Indeed, the solid state electrochemical replacement is especially favored in the case of small (<11 nm) and less stable Au NPs, becoming in these cases a viable mechanism for the formation of the thermodynamically stable ternary phase observed. However, in the case of larger and more stable Au NPs (25 nm), the system prefers to increase its thermodynamic stability through the homo-attachment of Au NPs (aggregation) rather than by hetero-attachment and the subsequent formation of a stable ternary phase. A similar unexpected solid-state replacement was observed by some of us during the transformation of Au−CdS nanostructures into Cd−Au_2S hybrid NPs.[43] However, in that case, the process took place only under the effect of the electron beam of the

https://doi.org/10.1021/acs.chemmater.2c01838
Chem. Mater. 2022, 34, 10849−10860

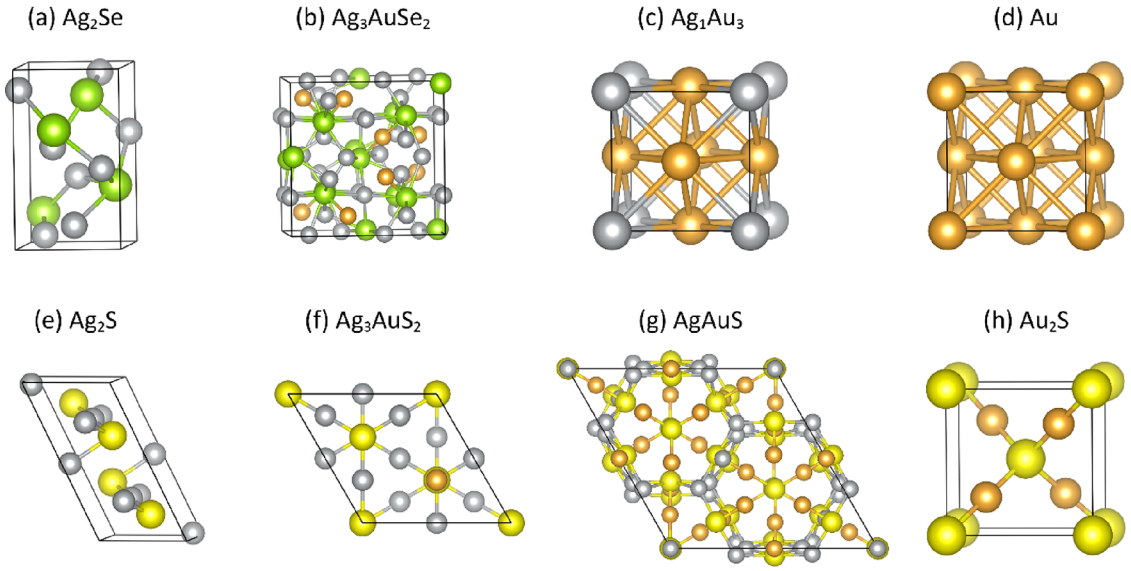

Figure 8. Structural models $(Ag, Au)_2Se$ and $(Ag, Au)_2S$ compounds as well as Au and Ag_1Au_3 metallic phases. Gold, silver, green, and yellow spheres depict Au, Ag, Se, and S atoms, respectively. The boundaries of the unit cells are indicated with solid black lines.

TEM, evidencing the high activation energy associated to the transformation. In contrast, the electrochemical replacement described in this work occurs spontaneously at room temperature with no specific energy input, making it kinetically feasible at room temperature.

Atomistic First Principles Calculations. Density functional theory (DFT) calculations were carried out to investigate the relative thermodynamic stability of the phases involved in the process. The calculations were performed using the VASP code[29,30] using the PBE functional[33] for total energy calculations of the fully relaxed structures and using the HSE06 functional[35] for the calculations of the band gaps of ternary phases, as detailed in the Computational Section. An overview of the phases considered in the calculations is provided in Table S3, and the unit cells of the considered phases as obtained after full relaxation are shown in Figure 8.

From the calculated total energies, the relative thermodynamic stability of the ternary phases (*fischesserite*, *uytenbogaardite*, and *petrovskaite*) was evaluated, starting with *fischesserite* Ag_3AuSe_2.

Assuming that the *fischesserite* phase is formed from Ag_2Se and Au, the energy gain associated with the formation of this phase can be evaluated from the reaction formulas listed in Table 1. With these reactions, various possibilities are considered for the Ag atoms that are expelled from the Ag_2Se compound and replaced with Au where pure Ag, AgAu, and $AgAu_3$ may be formed. The energies at the right-hand side of Table 1 show that the formation of pure Ag and AgAu as products would be favorable but the formation of an $AgAu_3$ alloy phase is most favorable. This agrees well with the experimental EDS observations showing that the metallic Au nanodomain also contains a considerable fraction of Ag.

Table 1. Change in the Potential Energy associated with the Formation of *Fischesserite* Ag_3AuSe_2 from Ag_2Se and Au

reaction formula	ΔE (eV)
$2(Ag_2Se) + Au \rightarrow Ag_3AuSe_2 + Ag$	−0.230
$2(Ag_2Se) + 2Au \rightarrow Ag_3AuSe_2 + AgAu$	−0.242
$2(Ag_2Se) + 4Au \rightarrow Ag_3AuSe_2 + AgAu_3$	−0.302

Second, the relative stability of the ternary sulfur compounds *uytenbogaardite* and *petrovskaite* was considered. Which phases are thermodynamically stable in the Ag−Au−S system depends on the relative concentrations of Ag, Au, and S. As *uytenbogaardite* and *petrovskaite* both have a cation/anion ratio of 2, to determine their thermodynamic stability, we have considered a subset of the Ag−Au−S system that can be described with the composition $(Ag_{1-x}Au_x)_2S$. Within this subset, the compositional extremes for $x = 0$ and $x = 1$ correspond to the well-known Ag_2S and Au_2S phases, and the formation energies of the *uytenbogaardite* and *petrovskaite* phases can be defined with respect to the energies of the Ag_2S and Au_2S phases:

$$E_{\text{form}}\{(Ag_{1-x}Au_x)_2S\} = E\{(Ag_{1-x}Au_x)_2S\} - (1-x)\cdot E\{Ag_2S\} - x\cdot E\{Au_2S\} \quad (2)$$

The formation energies thus obtained are listed in Table S4 and plotted in Figure S8. The energy of the *petrovskaite* phase is above the common tangent line, implying that the phase is not stable with respect to decomposition into *uytenbogaardite* and Au_2S. The energy differences are very small, however, that is, less than 10 meV/atom, indicating that all these phases are relatively stable at the respective compositions (Ag/Au ratios). It is also clear from Table S4 and Figure S8 that the compositional variations of the *petrovskaite* phase that were considered are energetically unfavorable in comparison with the standard composition AgAuS of this phase.

The DFT total energy calculations show that the formation of the three ternary phases is either favorable (*fischesserite* from Ag_2Se and Au) or likely to occur (*uytenbogaardite* and *pertrovskaite* from Ag_2S and Au). We mention here that only bulk unit cells have been considered in the DFT calculations. At the nanoscale, surface and interface energies are of importance as well and can very well stabilize a particular

https://doi.org/10.1021/acs.chemmater.2c01838
Chem. Mater. 2022, 34, 10849−10860

phase that is expected to be less stable when considering only bulk formation energies.

All in all, the experimental data, together with the results obtained by theoretical calculations, suggest that the formation of a kinetically favored and thermodynamically stable ternary phase (Ag_3AuX_2) is the main driving force promoting the formation of hybrid NPs.

To explore the functional potential of the ternary phases for optoelectronic applications, we also calculated the electronic band gap of these phases using the more advanced HSE06 functional (see the Characterization Methods section). From the values of the band gaps, as listed in Table 2, it becomes clear that *fischesserite* is predicted to be a narrow-band-gap semiconductor, while *uytenbogaardite* and *petrovskaite* have band gaps corresponding to blue and red wavelengths in the visible spectrum.

Table 2. Electronic Band Gaps Calculated Using HSE06

compound	phase	band gap (eV)
Ag_3AuSe_2	*fischesserite*	0.66
Ag_3AuS_2	*uytenbogaardite*	2.49
AgAuS	*petrovskaite*	1.61

The measurements for optical absorption of both samples were carried out in solution in the visible range. As shown in Figure 9, both samples show a gradually increasing absorption profile and a broad absorption band centered between 500 and 600 nm, which is characteristic of the localized surface plasmon resonance of colloidal Au.

CONCLUSIONS

In conclusion, the hetero-attachment of monometallic NPs and binary chalcogenide nanocrystals at room temperature and in solution is described, which leads to the formation of Au−Ag_2X hybrid NPs, where X = S, Se. The high thermodynamic stability and kinetic easiness of the formation of ternary phases and alloys at the nanoscale seem to be responsible for the high yield and selectivity of the hetero-attachment with respect to the homocoalescence of NPs. Indeed, upon the formation of the solid−solid interface between the two precursors Au and Ag_2X NPs, the growth of Au_3Ag and Ag_3AuX_2 domains occurs through solid-phase diffusion and electrochemical replacement through the interface, regardless of the standard redox potentials involved. The extension of the methodology to other technologically relevant materials is expected to enhance the consolidation of interfaces in solid nanostructured composites and thin films, improving in this way the transport properties in optoelectronic, thermoelectric, and catalytic devices.

ASSOCIATED CONTENT

Supporting Information

The Supporting Information is available free of charge at https://pubs.acs.org/doi/10.1021/acs.chemmater.2c01838.

Synthesis of 11 and 25 nm Au NPs, HR-(S)TEM micrographs for precursor NPs and hybrid Au−Ag_2Se NPs, characterization of the sample after obtaining by a reaction of Ag_2S NPs with 25 nm Au NPs, TEM micrograph of Au−Ag_2S hybrids obtained from Ag_2S NRs, interplanar distances found by HRTEM analysis in Au−Ag−S samples, TEM images for reaction mechanisms study of Au−Ag−S system, theoretical relative stability of the $(Ag, Au)_2S$ phases, TEM and XRD characterization for different Au−Ag−S samples, zeta-potential values for hydrophilic precursor samples, and parameters for DFT calculation and corresponding results (PDF)

AUTHOR INFORMATION

Corresponding Author

Albert Figuerola − *Department of Inorganic and Organic Chemistry, Inorganic Chemistry Section and Institute of Nanoscience and Nanotechnology, University of Barcelona, 08028 Barcelona, Spain;* orcid.org/0000-0003-1703-1025; Email: albert.figuerola@ub.edu

Authors

Mengxi Lin − *Department of Inorganic and Organic Chemistry, Inorganic Chemistry Section and Institute of Nanoscience and Nanotechnology, University of Barcelona, 08028 Barcelona, Spain*

Guillem Montana − *Department of Inorganic and Organic Chemistry, Inorganic Chemistry Section and Institute of Nanoscience and Nanotechnology, University of Barcelona, 08028 Barcelona, Spain;* Present Address: Fundació Institut de Recerca en Energia de Catalunya, Jardí de les dones de negre, no. 1-2a planta, 08930 Sant Adrià del Besòs Barcelona, Spain

Javier Blanco − *Institute of Nanoscience and Nanotechnology, University of Barcelona, 08028 Barcelona, Spain; Laboratory of Electron Nanoscopies (LENS-MIND), Department of Electronics and Biomedical Engineering, Universitat de Barcelona, 08028 Barcelona, Spain*

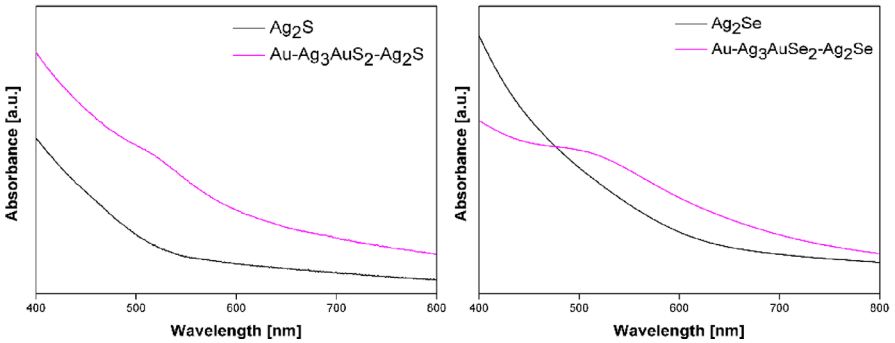

Figure 9. UV−vis absorption spectra of the Au−Ag_3S_2−Ag_2S sample compared to Ag_2S NPs (left) and the Au−Ag_3AuSe_2−Ag_2S sample compared to Ag_2Se NPs (right).

https://doi.org/10.1021/acs.chemmater.2c01838
Chem. Mater. 2022, 34, 10849−10860

Lluís Yedra − *Institute of Nanoscience and Nanotechnology, University of Barcelona, 08028 Barcelona, Spain; Laboratory of Electron Nanoscopies (LENS-MIND), Department of Electronics and Biomedical Engineering, Universitat de Barcelona, 08028 Barcelona, Spain*

Heleen van Gog − *Nanostructured Materials and Interfaces, Zernike Institute for Advanced Materials, University of Groningen, 9747 AG Groningen, Netherlands;* orcid.org/0000-0002-4824-0041

Marijn A. van Huis − *Soft Condensed Matter, Debye Institute for Nanomaterials Science, Utrecht University, 3584 CC Utrecht, Netherlands;* orcid.org/0000-0002-8039-2256

Miguel López-Haro − *Departamento de Ciencia de los Materiales e Ingeniería Metalúrgica y Química Inorgánica, Facultad de Ciencias, Universidad de Cádiz, Cádiz 11510, Spain;* orcid.org/0000-0003-2560-8015

José Juan Calvino − *Departamento de Ciencia de los Materiales e Ingeniería Metalúrgica y Química Inorgánica, Facultad de Ciencias, Universidad de Cádiz, Cádiz 11510, Spain;* orcid.org/0000-0002-0989-1335

Sònia Estradé − *Institute of Nanoscience and Nanotechnology, University of Barcelona, 08028 Barcelona, Spain; Laboratory of Electron Nanoscopies (LENS-MIND), Department of Electronics and Biomedical Engineering, Universitat de Barcelona, 08028 Barcelona, Spain*

Francesca Peiró − *Institute of Nanoscience and Nanotechnology, University of Barcelona, 08028 Barcelona, Spain; Laboratory of Electron Nanoscopies (LENS-MIND), Department of Electronics and Biomedical Engineering, Universitat de Barcelona, 08028 Barcelona, Spain;* orcid.org/0000-0002-5697-0554

Complete contact information is available at: https://pubs.acs.org/10.1021/acs.chemmater.2c01838

Author Contributions

M.L. and G.M. prepared and characterized all the samples. H.v.G. and M.A.v.H. performed the DFT calculations. J.B., M.L.-H., and L.Y. conducted the electron tomography and EDS experiments L.Y. contributed the analysis of the HR(S)TEM results. S.E., J.J.C., and F.P. coordinated and reviewed the TEM work. A.F. supervised the work and coordinated all contributions. The manuscript was written through contributions of all authors. All authors have given approval to the final version of the manuscript.

Notes

The authors declare no competing financial interest.

■ ACKNOWLEDGMENTS

A.F. acknowledges financial support from the Spanish Ministerio de Ciencia e Innovación (MICINN) through no. PID2019-106165GB-C22 and from the regional Generalitat de Catalunya authority (no. 2017 SGR 15). A.F. is a Serra Húnter fellow. L.Y. acknowledges financial support from the Spanish Ministerio de Ciencia e Innovación (MICINN) through the Juan de la Cierva Incorporación grant no. IJC2018-037698-I. J.B., S.E., and F.P. from the Consolidated Research Group of the "Generalitat de Catalunya" MIND (Micro-nanotechnology and Nanoscopies for Electronic and Photonic Devices) (2017 SGR 776) acknowledge the financial support from the Spanish Ministery of Science and Innovation (MICINN) through project no. PID2019-106165GB-C21, the Spanish Research Network no. RED2018-102609-T, and the FI-AGAUR Research Fellowship Program, Generalitat de Catalunya (FI grant no. 2018FI_B_00360). This work was also co-financed by the 2014−2020 ERDF Operational Programme and the Department of Economy, Knowledge, Business and University of the Regional Government of Andalusia, project reference no. FEDER-UCA18-107139.

■ REFERENCES

(1) Hurst, S. J.; Payne, E. K.; Qin, L.; Mirkin, C. A. Multisegmented One-Dimensional Nanorods Prepared by Hard-Template Synthetic Methods. *Angew. Chem., Int. Ed.* **2006**, *45*, 2672−2692.

(2) Cozzoli, P. D.; Pellegrino, T.; Manna, L. Synthesis, Properties and Perspectives of Hybrid Nanocrystal Structures. *Chem. Soc. Rev.* **2006**, *35*, 1195−1208.

(3) Cortie, M. B.; Mcdonagh, A. M. Synthesis and Optical Properties of Hybrid and Alloy Plasmonic Nanoparticles. *Chem. Rev.* **2011**, *111*, 3713−3735.

(4) Banin, U.; Ben-Shahar, Y.; Vinokurov, K. Hybrid Semiconductor−Metal Nanoparticles: From Architecture to Function. *Chem. Soc. Rev.* **2014**, *26*, 97−110.

(5) He, G.; Zhang, Y.; He, Q. MoS2/CdS Heterostructure for Enhanced Photoelectrochemical Performance under Visible Light. *Catalysts* **2019**, *9*, 19−21.

(6) Wang, H.; Gao, Y.; Liu, J.; Li, X.; Ji, M.; Zhang, E.; Cheng, X.; Xu, M.; Liu, J.; Rong, H.; Chen, W.; Fan, F.; Li, C.; Zhang, J. Efficient Plasmonic Au/CdSe Nanodumbbell for Photoelectrochemical Hydrogen Generation beyond Visible Region. *Adv. Energy Mater.* **2019**, *9*, No. 1803889.

(7) Rudenko, V.; Tolochko, A.; Zhulai, D.; Klimusheva, G.; Mirnaya, T.; Yaremchuk, G.; Asaula, V. Nonlinear Optical Properties of Metal Alkanoate Composites with Hybrid Core/Shell Nanoparticles. *Appl. Nanosci.* **2018**, *8*, 823−829.

(8) Carbone, L.; Cozzoli, P. D. Colloidal Heterostructured Nanocrystals: Synthesis and Growth Mechanisms. *Nano Today* **2010**, *5*, 449−493.

(9) Caro, C.; Dalmases, M.; Figuerola, A.; García-Martín, M. L.; Leal, M. P. Highly Water-Stable Rare Ternary Ag-Au-Se Nanocomposites as Long Blood Circulation Time X-Ray Computed Tomography Contrast Agents. *Nanoscale* **2017**, *9*, 7242−7251.

(10) Wang, Y.; Zhang, P.; Mao, X.; Fu, W.; Liu, C. Seed-Mediated Growth of Bimetallic Nanoparticles as an Effective Strategy for Sensitive Detection of Vitamin C. *Sens. Actuators, B* **2016**, *231*, 95−101.

(11) Xia, Y.; Gilroy, K. D.; Peng, H.-C.; Xia, X. Seed-Mediated Growth of Colloidal Metal Nanocrystals. *Angew. Chem., Int. Ed.* **2017**, *56*, 60−95.

(12) Qiao, S.; Yang, Z.; Xu, J.; Wang, X.; Yang, J.; Hou, Y. Chemical Synthesis, Structure and Magnetic Properties of Co Nanorods Decorated with Fe_3O_4 Nanoparticles. *Sci. China Mater.* **2018**, *61*, 1614−1622.

(13) Hodges, J. M.; Morse, J. R.; Fenton, J. L.; Ackerman, J. D.; Alameda, L. T.; Schaak, R. E. Insights into the Seeded-Growth Synthesis of Colloidal Hybrid Nanoparticles. *Chem. Mater.* **2017**, *29*, 106−119.

(14) Burrows, N. D.; Harvey, S.; Idesis, F. A.; Murphy, C. J. Understanding the Seed-Mediated Growth of Gold Nanorods through a Fractional Factorial Design of Experiments. *Langmuir* **2017**, *33*, 1891−1907.

(15) Kim, M.; Phan, V. N.; Lee, K. Exploiting Nanoparticles as Precursors for Novel Nanostructure Designs and Properties. *CrystEngComm* **2012**, *14*, 7535−7548.

(16) Deshmukh, S. D.; Ellis, R. G.; Sutandar, D. S.; Rokke, D. J.; Agrawal, R. Versatile Colloidal Syntheses of Metal Chalcogenide Nanoparticles from Elemental Precursors Using Amine-Thiol Chemistry. *Chem. Mater.* **2019**, *31*, 9087−9097.

(17) Vasquez, Y.; Henkes, A. E.; Chris Bauer, J.; Schaak, R. E. Nanocrystal Conversion Chemistry: A Unified and Materials-General

Strategy for the Template-Based Synthesis of Nanocrystalline Solids. *J. Solid State Chem.* **2008**, *181*, 1509−1523.
(18) Fayette, M.; Robinson, R. D. Chemical Transformations of Nanomaterials for Energy Applications. *J. Mater. Chem. A* **2014**, *2*, 5965−5978.
(19) Chen, X.; Fuchs, H.*Soft Matter Nanotechnology : From Structure to Function*; Wiley-VCH Verlag GmbH & Co. KGaA: Weinheim, 2015.
(20) de Trizio, L.; Manna, L. Forging Colloidal Nanostructures via Cation Exchange Reactions. *Chem. Rev.* **2016**, *116*, 10852−10887.
(21) Park, J.; Lim, S.; Kwon, T.; Jun, M.; Oh, A.; Baik, H.; Lee, K. Longitudinal Strain Engineering of $Cu_{2-x}S$ by the Juxtaposed Cu_5FeS_4 Phase in the $Cu_5FeS_4/Cu_{2-x}S/Cu_5FeS_4$ Nanosandwich. *Chem. Mater.* **2019**, *31*, 9070−9077.
(22) Hinterding, S. O. M.; Berends, A. C.; Kurttepeli, M.; Moret, M. E.; Meeldijk, J. D.; Bals, S.; van der Stam, W.; de Mello Donega, C. Tailoring Cu^+ for Ga^{3+} Cation Exchange in $Cu_{2-X}S$ and $CuInS_2$ Nanocrystals by Controlling the Ga Precursor Chemistry. *ACS Nano* **2019**, *13*, 12880−12893.
(23) Zhang, L.; Xu, L.; Zhu, M.; Li, C.; Li, L.; Su, J.; Gao, Y. Pink All-Inorganic Halide Perovskite Nanocrystals with Adjustable Characteristics: Fully Reversible Cation Exchange, Improving the Stability of Dopant Emission and Light-Emitting Diode Application. *J. Alloys Compd.* **2019**, No. 152913.
(24) Suri, M.; Hazarika, A.; Larson, B. W.; Zhao, Q.; Vallés-Pelarda, M.; Siegler, T. D.; Abney, M. K.; Ferguson, A. J.; Korgel, B. A.; Luther, J. M. Enhanced Open-Circuit Voltage of Wide-Bandgap Perovskite Photovoltaics by Using Alloyed $(FA_{1-x}Cs_x)Pb(I_{1-x}Br_x)_3$ Quantum Dots. *ACS Energy Lett.* **2019**, *4*, 1954−1960.
(25) Dalmases, M.; Ibáñez, M.; Torruella, P.; Fernàndez-Altable, V.; López-Conesa, L.; Cadavid, D.; Piveteau, L.; Nachtegaal, M.; Llorca, J.; Ruiz-González, M. L.; Estradé, S.; Peiró, F.; Kovalenko, M. v.; Cabot, A.; Figuerola, A. Synthesis and Thermoelectric Properties of Noble Metal Ternary Chalcogenide Systems of Ag-Au-Se in the Forms of Alloyed Nanoparticles and Colloidal Nanoheterostructures. *Chem. Mater.* **2016**, *28*, 7017−7028.
(26) Dalmases, M.; Torruella, P.; Blanco-Portals, J.; Vidal, A.; Lopez-Haro, M.; Calvino, J. J.; Estradé, S.; Peiró, F.; Figuerola, A. Gradual Transformation of Ag_2S to Au_2S Nanoparticles by Sequential Cation Exchange Reactions: Binary, Ternary, and Hybrid Compositions. *Chem. Mater.* **2018**, *30*, 6893−6902.
(27) Wang, J.; Feng, H.; Chen, K.; Fan, W.; Yang, Q. Solution-Phase Catalytic Synthesis, Characterization and Growth Kinetics of Ag_2S-CdS Matchstick-like Heteronanostructures. *Dalton Trans.* **2014**, *43*, 3990−3998.
(28) Sahu, A.; Qi, L.; Kang, M. S.; Deng, D.; Norris, D. J. Facile Synthesis of Silver Chalcogenide (Ag_2E; E = Se, S, Te) Semiconductor Nanocrystals. *J. Am. Chem. Soc.* **2011**, *133*, 6509−6512.
(29) Kresse, G.; Furthmüller, J. Efficient Iterative Schemes for *Ab Initio* Total-Energy Calculations Using a Plane-Wave Basis Set. *Phys. Rev. B* **1996**, *54*, No. 11169.
(30) Kresse, G.; Furthmüller, J. Efficiency of Ab-Initio Total Energy Calculations for Metals and Semiconductors Using a Plane-Wave Basis Set. *Comput. Mater. Sci.* **1996**, *6*, 15−50.
(31) Kresse, G.; Joubert, D. From Ultrasoft Pseudopotentials to the Projector Augmented-Wave Method. *Phys. Rev. B* **1999**, *59*, 1758.
(32) Blöchl, P. E. Projector Augmented-Wave Method. *Phys. Rev. B* **1994**, *50*, 17953.
(33) Perdew, J. P.; Burke, K.; Ernzerhof, M. Generalized Gradient Approximation Made Simple. *Phys. Rev. Lett.* **1996**, *77*, 3865.
(34) Mikhlin, Y. L.; Nasluzov, V. A.; Romanchenko, A. S.; Shor, A. M.; Pal'Yanova, G. A. XPS and DFT Studies of the Electronic Structures of AgAuS and Ag_3AuS_2. *J. Alloys Compd.* **2014**, *617*, 314−321.
(35) Krukau, A. V.; Vydrov, O. A.; Izmaylov, A. F.; Scuseria, G. E. Influence of the Exchange Screening Parameter on the Performance of Screened Hybrid Functionals. *J. Chem. Phys.* **2006**, *125*, 224106.
(36) Sharma, R. C.; Chang, Y. A. The Ag−S (Silver-Sulfur) System. *Bull. Alloy Phase Diagr.* **1986**, *7*, 263−269.
(37) Wang, J.; Fan, W.; Yang, J.; Da, Z.; Yang, X.; Chen, K.; Yu, H.; Cheng, X. Tetragonal - Orthorhombic - Cubic Phase Transitions in Ag_2Se Nanocrystals. *Chem. Mater.* **2014**, *26*, 5647−5653.
(38) Schoen, D. T.; Xie, C.; Cui, Y. Electrical Switching and Phase Transformation in Silver Selenide Nanowires. *J. Am. Chem. Soc.* **2007**, *129*, 4116−4117.
(39) Kalsin, A. M.; Fialkowski, M.; Paszewski, M.; Smoukov, S. K.; Bishop, K. J. M.; Grzybowski, B. A. Electrostatic Self-Assembly of Binary Nanoparticle Crystals with a Diamond-like Lattice. *Science* **2006**, *312*, 420−424.
(40) Huang, Z.; Zhao, Z. J.; Zhang, Q.; Han, L.; Jiang, X.; Li, C.; Cardenas, M. T. P.; Huang, P.; Yin, J. J.; Luo, J.; Gong, J.; Nie, Z. A Welding Phenomenon of Dissimilar Nanoparticles in Dispersion. *Nat. Commun.* **2019**, *10*, 1−8.
(41) Xia, X.; Wang, Y.; Ruditskiy, A.; Xia, Y. 25th Anniversary Article: Galvanic Replacement: A Simple and Versatile Route to Hollow Nanostructures with Tunable and Well-Controlled Properties. *Adv. Mater.* **2013**, *25*, 6313−6333.
(42) Pattadar, D. K.; Masitas, R. A.; Stachurski, C. D.; Cliffel, D. E.; Zamborini, F. P. Reversing the Thermodynamics of Galvanic Replacement Reactions by Decreasing the Size of Gold Nanoparticles. *J. Am. Chem. Soc.* **2020**, *142*, 19268−19277.
(43) van Huis, M. A.; Figuerola, A.; Fang, C.; Béché, A.; Zandbergen, H. W.; Manna, L. Chemical Transformation of Au-Tipped CdS Nanorods into AuS/Cd Core/Shell Particles by Electron Beam Irradiation. *Nano Lett.* **2011**, *11*, 4555−4561.

https://doi.org/10.1021/acs.chemmater.2c01838
Chem. Mater. 2022, 34, 10849−10860